

# *In Situ* High-Resolution Transmission Electron Microscopy in the Study of Nanomaterials and Properties

James M. Howe, Hirotaro Mori, and  
Zhong Lin Wang

## Abstract

This article introduces the use of *in situ* high-resolution transmission electron microscopy (HRTEM) techniques for the study and development of nanomaterials and their properties. Specifically, it shows how *in situ* HRTEM (and TEM) can be used to understand diverse phenomena at the nanoscale, such as the behavior of alloy phase formation in isolated nanometer-sized particles, the mechanical and transport properties of carbon nanotubes and nanowires, and the dynamic behavior of interphase boundaries at the atomic level. Current limitations and future potential advances in *in situ* HRTEM of nanomaterials are also discussed.

## Introduction

It is often necessary to study nanoscale materials under the actual conditions in which they exist in order to understand their functionality, or the fundamental phenomena governing their behavior in realistic environments. As materials systems continue to decrease in size, the capability to study these materials at the highest possible levels of spatial resolution is becoming increasingly important. *In situ* high-resolution transmission electron microscopy (HRTEM) enables such studies and can be applied to a variety of nanoscale materials phenomena.

HRTEM imaging is a phase-contrast dominated imaging technique where two or more beams are allowed to interfere to

form an image. Because the lens system of the TEM must preserve the coherence of the image-forming beams, the spacing being resolved in the image must be within the resolution limits of the microscope. This requirement generally limits HRTEM to observations of projected specimen structures along relatively low-index zone axes with wide interplanar spacings that are within the resolution limits of the microscope. Under optimum conditions, an HRTEM image can be directly interpreted as a map of the projected crystal structure (crystal potential) along the electron-beam direction. Such interpretation is usually possible only for a narrow range of specimen and microscope parameters, but this

situation and its variations are well understood. In any case, the resulting HRTEM image is a two-dimensional projection of the three-dimensional structure, with the columns (or planes) of atoms being either dark or bright, depending on the exact specimen and imaging conditions.

The specimen and microscope requirements for *in situ* HRTEM imaging are not generally different from those of usual HRTEM, except that one must have specialized holders capable of inducing changes in the specimen and some method of recording and analyzing the resulting dynamic responses. Many different types of holders capable of heating or cooling, straining, lasing, evaporating/depositing, applying a current/voltage, etc., are available commercially or can be fabricated without great difficulty. Some of these holders are mentioned in the following examples. At present, most HRTEMs are equipped with a charge-coupled device (CCD) or television (TV)-rate cameras that are fiber-optically coupled to the HRTEM for recording high-resolution images at 30 frames/s. Specimen drift caused by temperature changes that lead to expansion or bending of the sample or sample holder is usually not a significant problem when inducing small changes to a specimen and images are being acquired at TV rates. If substantial drift does occur, it can make subsequent interpretation and/or computer comparison of the resulting digital images difficult. Drift is a critical limiting factor for HRTEM imaging in a scanning transmission electron microscope (STEM), so most *in situ* experiments have so far been performed in TEMs; this article focuses on examples from TEM and HRTEM techniques. The examples discussed in this article illustrate the wealth and variety of information that can be obtained about nanomaterials and processes by employing *in situ* studies.

## Applications

### ***Alloy Phase Formation in Isolated Nanometer-Sized Particles***

Nanometer-sized materials are very attractive for a variety of applications because they exhibit properties that are significantly different from those of the corresponding bulk materials. In the design and application of these materials, understanding the basic rule for alloy phase formation under dimensional constrictions is important. Recent remarkable progress in *in situ* HRTEM makes it possible to directly observe the alloy phase formation process as a function of temperature, size, and composition.<sup>1</sup>

It is clear that a large reduction of the eutectic temperature takes place with

decreasing size of alloy particles.<sup>2</sup> Figure 1a shows an as-produced Sn particle containing an amount of In. Lattice fringes seen in the particle indicate that the particle is in a crystalline state and therefore in the state of a solid solution. The formation of facets can be clearly recognized on the surface of the particle. The temperature of the graphite substrate was kept at room temperature. With continued deposition of In, all the lattice fringes abruptly disappeared, and at the same time the shape of the particle changed from faceted and polygonal to round and semispherical, as seen in Figure 1b. No salt and pepper contrast characteristic of an amorphous solid was present in the particle. These observations indicate that the droplet is in a liquid state. The In concentration in the liquid particle was approximately 55 at.% In. Therefore, the stable phase of the approximately 7-nm-sized Sn-55 at.% In alloy particle at room temperature is liquid; this is in sharp contrast with the equilibrium phase(s) in bulk material (i.e., a two-phase mixture of  $\text{In}_3\text{Sn}$  and  $\text{InSn}_4$ ).<sup>3</sup> The eutectic temperature of the Sn-In system in bulk is reported to be 393 K.<sup>3</sup> Figure 1b shows, therefore, the eutectic temperature was depressed by more than 100 K when the size of the system is reduced from bulk to ~7 nm. This large depression arises because the contribution of the interfacial energy between two different solid phases to the total Gibbs free energy of the particle becomes so high that the eutectic temperature is lowered much faster than the melting point of the pure components with decreasing particle size.<sup>1</sup>

The second example concerns the change in microstructure with composition at temperatures above the eutectic temperature. Figure 2 shows a typical sequence of the alloying process of Sn into a nanometer-sized Bi particle at around 350 K.<sup>4</sup> Figure 2a shows an as-produced pure Bi particle on the graphite substrate. The size of the particle was approximately 8 nm. Figure 2b shows the same particle after Sn deposition. By the deposition of Sn the structure of the particle changed from a single crystal to a mixture of crystalline and liquid phases, as seen from Figure 2b. The interface between the crystalline and the liquid phase (double arrowed) was rather smooth. A faceted surface of the crystalline Bi (shown in Figure 2a) was replaced by a round curved surface of the liquid phase (arrowed). With continued deposition of Sn, the crystal-liquid interface moved left and downward at the expense of the crystal (Figures 2b-d), and eventually the whole particle became liquid (Figure 2e). Figure 2f is an energy-dispersive x-ray spectrum taken from the central portion of the particle depicted in Figure 2e, showing that the composition of the particle

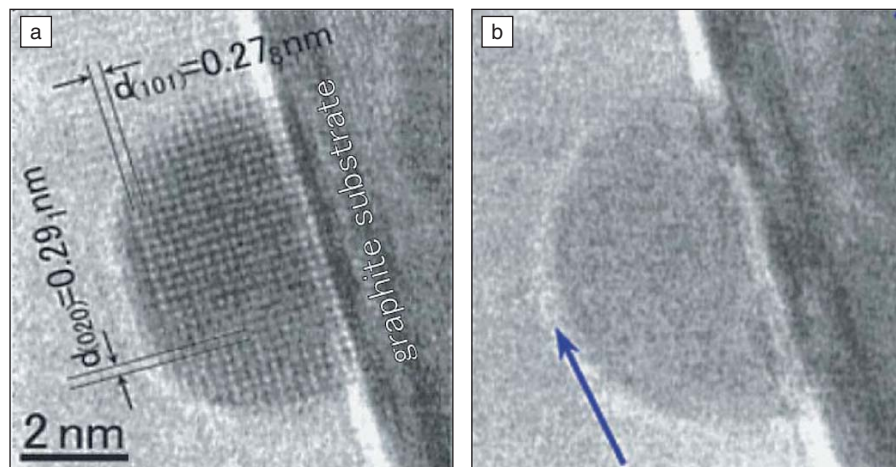


Figure 1. Large depression of the eutectic temperature of a nanometer-sized Sn-In alloy particle. (a) As-produced Sn-In alloy particle in a state of a solid solution, (b) the same particle, which underwent a melting transition by additional alloying of In. During the experiment, the temperature of the substrate was kept at room temperature (from Reference 2). Subscripted numbers in plane spacing values indicate uncertainty in that decimal space.

was Bi-50 at.% Sn. The change in the microstructure with the composition mentioned above (i.e., a heterogeneous mechanism: crystalline → crystalline + liquid → liquid) is consistent with that predicted from the phase diagram for the bulk material at temperatures between the eutectic temperature and the melting point of Bi.<sup>3</sup> However, this microstructural change with composition is altered when the size of particles is further reduced down to the 5 nm range. Namely, a 5-nm-sized Bi particle underwent an abrupt crystalline-to-liquid phase change in the course of continuous alloying of Sn at around 350 K.<sup>5</sup> In the abrupt phase change, no formation and movement of a crystal-liquid interface was detected. This type of phase change (i.e., a homogeneous mechanism) is in sharp contrast to the manner observed in a relatively large-sized (8-nm-sized) particle shown in Figure 2 (i.e., a heterogeneous mechanism). Thermodynamic model calculations indicate that such alteration in the phase change from a heterogeneous to homogeneous mechanism with decreasing particle size can be consistently explained in terms of the contribution of the solid-liquid interfacial energy.<sup>4</sup>

Last, it is worth mentioning that *in situ* HRTEM also plays a key role in revealing the significant enhancement of the solid solubility in nanometer-sized alloy particles.<sup>6</sup>

**In Situ TEM and HRTEM of Nanotubes and Nanowires**  
**In Situ Nanomechanics of One-Dimensional Nanomaterials.** TEM is powerful for characterizing the atomic and electronic structure of inorganic materials.

In recent years, *in situ* measurement techniques using the high spatial resolution provided by TEM have been extensively developed for directly imaging the local structure while its properties are being measured. The pioneer work of measuring the elastic modulus of a single carbon nanotube is an outstanding example.<sup>7,8</sup> Inspired by this work, improved specimen holders and manipulation stages have been developed for *in situ* characterization of the mechanical, electrical, and field emission properties of nanotubes (NTs), nanowires (NWs), and nanobelts (NBs). By applying an alternating voltage across an electrode and an NT, mechanical resonance is induced when the externally applied frequency matches the natural resonance frequency of the NT (see Figure 3). If the size of the measured object is relatively large (greater than 10–20 nm as a first approximation, depending on the material and conditions) so that classical elasticity theory still holds, quantifying the resonance frequency gives the elastic modulus of the NT. Such an experiment can be easily done in a scanning electron microscope because of the large-size specimen chamber and three-dimensional manipulation.<sup>9</sup>

TEM is most powerful for direct imaging of dislocations in solid materials and is ideally suited for studying plastic deformation of NWs. An *in situ* technique has been developed for conducting bending or axial tensile experiments for NWs and NTs in the TEM.<sup>10,11</sup> The technique relies on the deformation produced by a partially broken carbon film on which NWs are attached. The stretching of the carbon film as illuminated by the electron beam

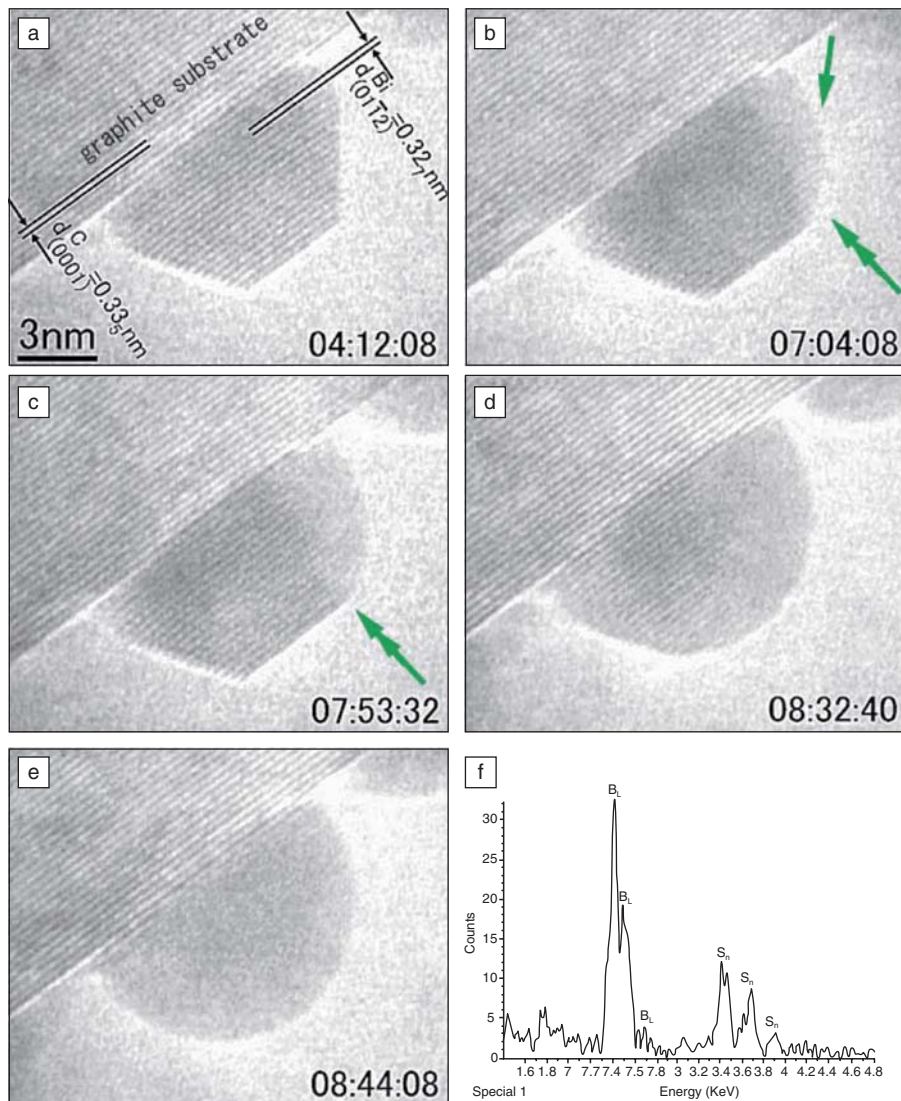


Figure 2. A sequence from a video recording of the alloying process of Sn into a nanometer-sized Bi particle: (a) as-produced Bi particle on the graphite substrate; (b–e) the same particle under a Sn deposition condition. With Sn deposition, a crystalline–liquid interface formed in the particle (double arrowed in b), and it then moved left and downward at the expense of the crystal (see c and d) until the whole particle became liquid (e). The three numbers inserted in each micrograph indicate the time in units of minutes, seconds, and one-sixtieth seconds (from Reference 4).

results in the tensile stretching of an NW. Using this technique, unusually large-strain plasticity of ceramic SiC NWs at room temperature has been directly observed (Figure 4). The continuous plasticity of the SiC NWs is accompanied by a process of increased dislocation density at early stages, followed by an obvious lattice distortion, and finally reaches an entire structure amorphization at the most strained region of the NW. These unusual phenomena for the SiC NWs are fundamentally important for understanding the nanoscale fracture and strain-

induced band structure variation for high-temperature semiconductors.<sup>10</sup> A diameter reduction as large as 426% (the ratio of incipient diameter over the breakpoint diameter [%]) and 125% elongation were obtained at ambient temperature for Si NWs.<sup>11</sup> Development of dislocations and their dynamics at the early stage of plastic deformation was directly imaged.

***In Situ* Transport Property of One-Dimensional Nanomaterials.** The conductance measurement of individual carbon NTs has also been carried out using

an *in situ* TEM technique, employing a specimen holder that is able to manipulate the position of the NT so that it can be in a good contact with a counter electrode that is mechanically soft enough to make an Ohmic contact. The idea is to apply a voltage across the NT and measure its current–voltage ( $I$ – $V$ ) characteristics when its structure is continuously imaged by TEM. This allows a direct correlation between the observed structural changes with the measured  $I$ – $V$  characteristics. Figure 5a shows an NT that is in contact with a carbon electrode and a Hg electrode. After applying a large current, the end that was in contact with Hg was locally burnt off, possibly because of the large local contact resistance (Figure 5b). Using this *in situ* TEM technique, the detailed conditions under which the ballistic quantum conductance of a multi-walled NT was observed has been studied.<sup>12</sup>

*In situ* TEM is also powerful for studying the electromechanical coupling response of one-dimensional (1D) nanomaterials, such as boron nitride (BN) tubes.<sup>13,14</sup> Using a specimen stage that can apply a strain to an NT and continuously monitor its electrical transport property, the electromechanical coupled property can be characterized, provided the contacts between the NT and the electrodes are Ohmic with negligible contact resistance.<sup>15,16</sup> This technique enables direct correlation between the transport properties with the local strain and deformation built in the NT, thus providing a great technique for investigating the electromechanical coupled properties of a NT.

***In Situ* Field Emission of One-Dimensional Nanomaterials.** *In situ* TEM is capable of directly mapping the electric field distribution around an NT tip when it is emitting electrons. The mapping is based on electron holography, which is sensitive to the phase shift of the incident electron as introduced by the local electrostatic potential around the NT tip.<sup>17</sup> Due to the large aspect ratio of 1D nanomaterials, the electric field at their tips can be rather large, thus the local temperature could be very high during field emission. It is possible to induce structural damage at the tips. TEM is ideal for directly observing the structural damage of a carbon NT during field emission under a higher voltage.<sup>18</sup> The damage occurs in a way that the walls of the NTs are split piece-by-piece and segment-by-segment. The mechanisms of the field-induced damage are believed to be caused by two processes. One, the electrostatic force acting on the tip of the NT can split the NT piece-by-piece and segment-by-segment. The second process is likely

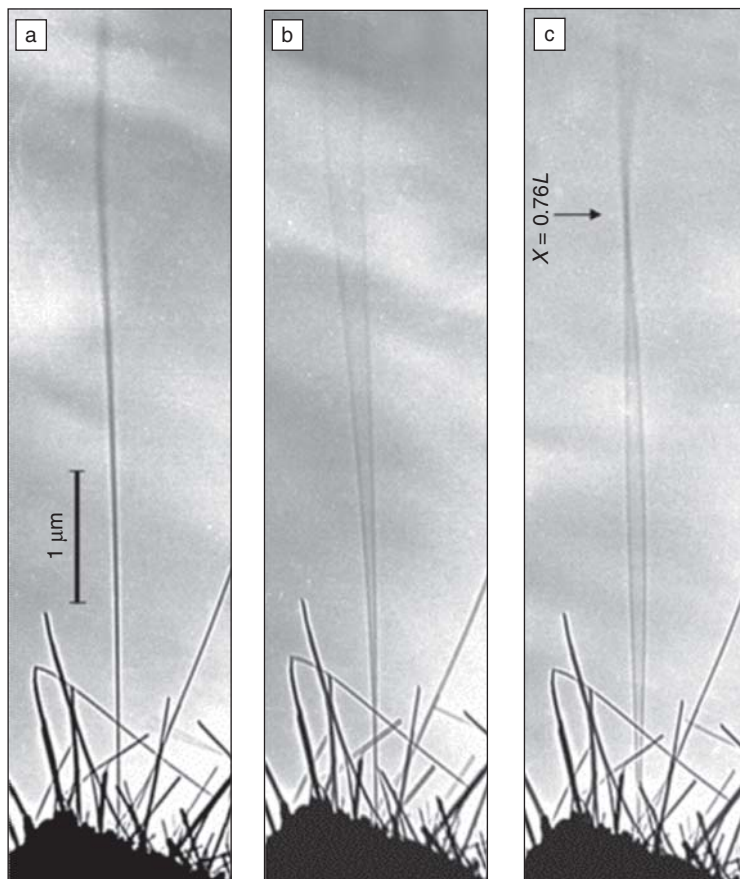


Figure 3. Nanotube response to resonant alternating applied potentials. (a) In the absence of a potential, the nanotube tip (length  $L = 6.25 \mu\text{m}$ , diameter  $D = 14.5 \text{ nm}$ ) vibrated slightly because of thermal effects. (b) Resonant excitation of the fundamental mode of vibration (frequency  $\nu_1 = 0.53 \text{ MHz}$ ); the shape corresponds closely to that expected for a cantilevered uniform beam. (c) Resonant excitation of the second harmonic (frequency  $\nu_2 = 3.01 \text{ MHz}$ ).

due to the local temperature created by the flow of emission current, which may “burn” the NT layer-by-layer. Recent calculations by Wei et al.<sup>19</sup> suggest that the highest temperature along an NT during field emission is not at the tip but at a short distance away from the tip because of the enhanced emission rate at the tip that takes away some local heat; this may explain the segment-by-segment damage of the NT.

An important physical quantity in electron field emission is the surface work function, which is well documented for elemental materials. For emitters such as carbon NTs, most of the electrons are emitted from the tips of the carbon NTs, and it is the local work function that matters to the properties of NT field emission. A technique has been developed to measure the work function at the tip of a single carbon NT.<sup>20</sup> The measurement is based on the electric-field-induced mechanical resonance of the NT. The field emission of an NT has

been directly correlated to the structure at the tip, thus providing a quantitative understanding about the characteristics of NT field emission and its dependence on local tip structure.<sup>21,22</sup>

### In Situ HRTEM of Interphase Boundary Dynamics

Understanding how atoms arrange at interphase boundaries and cross from one phase to the other is essential to understanding the nature of phase transformations in materials.<sup>23,24</sup> Phase transformations are important, because they are one of the main techniques that materials scientists employ to develop materials structures with sizes ranging from a few atoms to micrometers.<sup>25</sup> Since interphase boundaries are internal interfaces, *in situ* hot-stage HRTEM is one of the few techniques capable of providing both atomic-level structural and dynamic information about such

interfaces. This section illustrates how *in situ* hot-stage HRTEM can be used to determine the dynamic behavior of interphase boundaries at the atomic level, focusing on a diffuse coherent interphase boundary in a Au-Cu alloy.

Figure 6a shows an HRTEM image of a diffuse interphase boundary between the long-range ordered (O) AuCu-I phase and disordered (D)  $\alpha$  phase in a Au-41Cu (at.%) alloy sample taken as a frame from a videotape at approximately 305°C during *in situ* heating in the HRTEM.<sup>26</sup> The position where a 25-pixel-wide intensity profile was taken across the interphase boundary is indicated by the white rectangle in the figure. The corresponding intensity (brightness) profile is shown in Figure 6b. In this profile, the ends of the diffuse interphase boundary on the ordered and disordered sides are indicated by the lines labeled O and D, respectively, and the same locations are also indicated in Figure 6a. Detailed HRTEM image simulations (e.g., inset in bottom left in Figure 6a) show that the Au-rich (001) planes in the ordered AuCu-I phase appear as bright lines in the image in Figure 6a and corresponding high intensity peaks on the left side of the intensity profile in Figure 6b. The Cu-rich planes between the peaks are barely visible because they appear dark in the HRTEM image in Figure 6a under these experimental conditions. The lower intensity peaks spaced only half this distance apart to the right of position D correspond to the {002} planes in the disordered  $\alpha$  phase. In the region between O and D, the intensities change from left to right, leading to the interphase boundary thickness labeled L in Figure 6b.

The positions O and D in Figure 6 were determined for each frame (time interval of 0.03 s) during a period of 60 s, and these are plotted in Figure 7a, which shows several important features. First, it is evident that the disordered side of the diffuse interphase boundary (top graph) generally moves more frequently and often over larger distances than the ordered side of the interphase boundary (bottom graph) with time. The smallest distance present in the top graph (arrow) is the spacing of one {002} plane in the disordered  $\alpha$  phase. Following the disordered side of the interphase boundary with time, it is evident that the interphase boundary fluctuates over a distance of one to six {002}  $\alpha$  planes. In contrast, using the {002} plane spacing as a reference, it is apparent that the ordered side of the interphase boundary in the lower graph typically moves twice this distance, which is the spacing between the

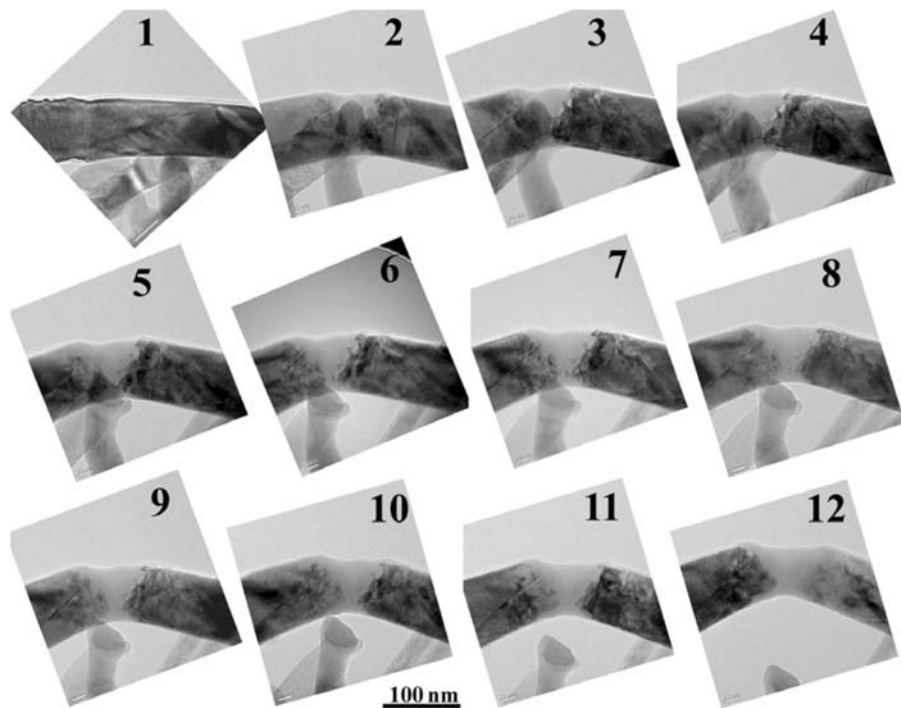


Figure 4. A series of transmission electron microscopy (TEM) images showing the bent SiC NWs from elastic (1) to plastic (2) and the large strain plasticity through 3 to 12. An amorphous character was directly observed in 3 and 12. The amorphous region shows transparent contrast in the middle, which is distinctive from the crystalline regions. (Image courtesy of X.D. Han and Z. Zhang, from Reference 10).

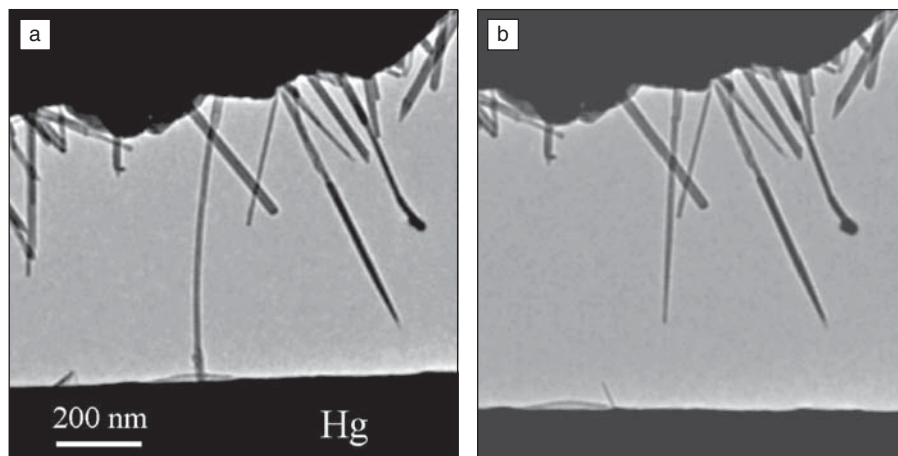


Figure 5. *In situ* observation of electric transport through single carbon nanotubes. (a) Applied voltage  $V = 0.1$  V, current  $I = 7.3$   $\mu$ A, the resistance of the carbon  $R = 12.7$  k $\Omega$  which corresponds to a conductance  $G = (12.7 \text{ k}\Omega)^{-1} = 1.02 G_0$  where  $G_0$  is the quantized conductance of a single conduction channel. (b) After applying a 4 V voltage, the nanotube was broken; the break occurred at the contact of the nanotube and the Hg.

Au-rich (001) planes in the AuCu-I phase. In addition, it fluctuates with a frequency that is several times less than that of the disordered side. Thus, the position of the disordered side of the interphase boundary rapidly fluctuates between a number

of adjacent {002}  $\alpha$  planes with time, whereas the ordered side fluctuates more slowly and only between Au-rich planes in the ordered AuCu-I phase.

The different interphase boundary behaviors observed in Figure 7a are likely

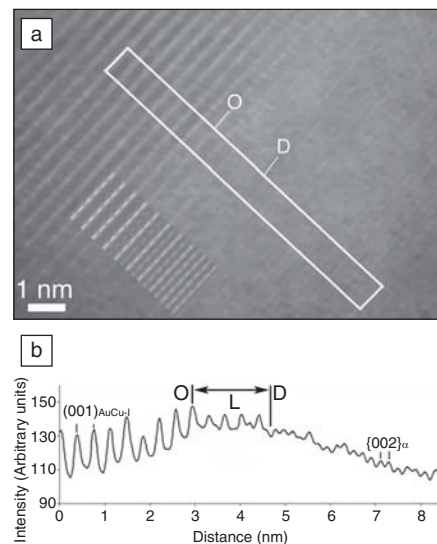


Figure 6. (a) High-resolution TEM image of an order–disorder interphase boundary at 305°C with a simulated image of the interphase boundary for the same sample and microscope conditions shown superimposed on the experimental image. The Au-rich (001) planes in the AuCu-I phase appear bright on the left side of the interphase boundary as do the {002} planes that are spaced approximately half as far apart in the  $\alpha$  phase on the right side. (b) A 25-pixel-wide intensity profile taken across the interphase boundary over the region indicated by a white box in (a). The positions O and D, which indicate the ordered and disordered sides of the diffuse interphase boundary, respectively, are indicated in both (a) and (b) (from Reference 26).

due to a combination of several factors occurring at the interphase boundary, namely: (1) the tetragonality of the AuCu-I structure, which leads to an energetically stable (001) plane that tends to keep the ordered side of the interphase boundary parallel to this plane, (2) a lower average diffusivity in the AuCu-I phase as compared to the disordered  $\alpha$  phase at 305°C, (3) a related longer atomic jump-distance (0.357 nm) for diffusion perpendicular to the ordered (001) planes in the AuCu-I ordered phase, and (4) the fact that the interphase boundary must move this same distance between Au-rich planes on the ordered side.<sup>27,28</sup> A combination of these effects leads to a significantly higher activation energy for movement of the ordered side of the interphase boundary, causing the experimentally observed interphase boundary behavior in Figure 7a. In fact, if one performs an approximate calculation for the average diffusivities and corresponding jump frequencies of

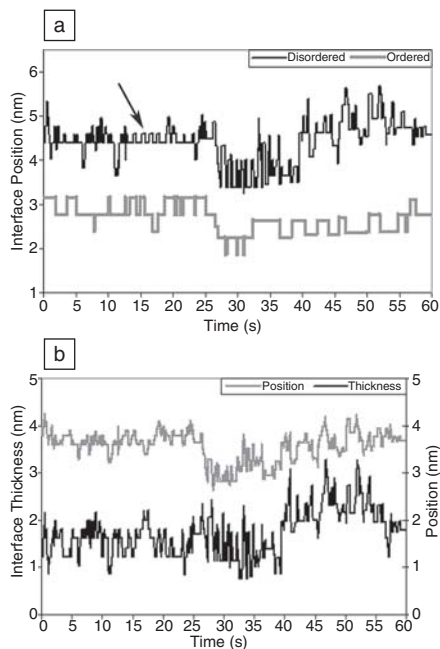


Figure 7. (a) Graphs showing the positions of the disordered (top) and ordered (bottom) sides of the diffuse interphase boundary in Figure 6a over a period of 60 s. (b) Corresponding graphs showing the interphase boundary mean position (top) and thickness (bottom) for the same period. The interphase boundary mean position in Figure 7b fluctuates around a value of approximately 3.5 nm, which is roughly the midpoint between the two intensity profiles in Figure 7a (from Reference 26).

the atoms in the ordered and disordered phases, respectively, using the equation  $\Gamma = 6D/\lambda^2$ , where  $\Gamma$  is the jump frequency ( $s^{-1}$ ),  $D$  is the diffusivity at 305°C of  $1.7 \times 10^{-15} \text{ m}^2/\text{s}$  for the  $\alpha$  phase and  $7.0 \times 10^{-16} \text{ m}^2/\text{s}$  for the AuCu-I phase,<sup>28</sup> and  $\lambda$  is the jump distance ( $3.7 \times 10^{-10} \text{ m}$  in AuCu-I), one finds that the jump frequency in the disordered phase is approximately  $3 \times 10^5 \text{ s}^{-1}$ , as compared to  $3 \times 10^4 \text{ s}^{-1}$  in the ordered phase, consistent with the considerations mentioned above. However, these frequencies are approximately four orders of magnitude greater than the actual frequencies of interphase boundary movement recorded for the ordered and disordered sides of the interphase boundary, indicating that collective atom volumes, rather than individual atom jumps, are involved in the process. In other words, movement of the interface involves the formation of critical-size fluctuations involving many atoms.<sup>29,30</sup>

The interphase boundary thickness and mean position were determined

from the data in Figure 7a and these are plotted in Figure 7b. The mean interphase boundary position was determined as the midpoint between positions O and D. The average frequency of interphase boundary movement is  $1.2 \text{ s}^{-1}$ , with a maximum frequency of  $7.7 \text{ s}^{-1}$  and a minimum frequency of  $0.4 \text{ s}^{-1}$ . This temporal variation reflects mainly that of the disordered side, which fluctuates at a higher frequency. Also note that the mean interphase boundary position moves up more often than down in Figure 7b, again reflecting the character of the disordered side of the interphase boundary, which tends to move into the disordered phase, expanding the interphase boundary. Thus, the interphase boundary fluctuations are not symmetric about the mean position, but favor the disordered side. The average velocities of the ordered and disordered sides of the interphase boundary were also determined over 60 s using the data in Figure 7a and were  $0.3 \text{ nm/s}$  and  $1.3 \text{ nm/s}$ , respectively.

The interphase boundary thickness is shown in the bottom graph in Figure 7b. The average thickness was approximately 1.7 nm, or the equivalent of 7 {002} planes (or  $\sim 4$  unit-cells) in the disordered  $\alpha$  phase, although the thickness averaged slightly more than 2.0 nm during the latter 20 s of the video sequence, where the disordered side of the interphase boundary moved a few planes farther away from the ordered side. The maximum and minimum interphase boundary thicknesses observed were 3.3 and 0.8 nm, respectively, which represent variations in thickness on the order of 100%. The average interphase boundary thickness measured from Figure 7b is comparable to recent studies on strain-induced incomplete wetting above the critical temperature  $T_c$ , where the alloy becomes disordered, at AuCu-I (001) surfaces,<sup>27</sup> and is also similar to previous calculations for a Au-Cu alloy<sup>31</sup> and recent atomistic calculations performed on Al-Li and Al-Ag alloys slightly below  $T_c$  using embedded atom potentials and Monte Carlo methods.<sup>32,33</sup> In the Al-based alloys, which behave similar to Au-Cu alloy, the calculations indicate that the diffuse interphase boundary should extend over 4–6 unit cells (i.e.,  $L \sim 1.6\text{--}2.4 \text{ nm}$ ), and the strain-induced incomplete wetting phenomenon leads to order in AuCu (001) surfaces that extends 5–7 planes (i.e.,  $L \sim 1.0\text{--}1.4 \text{ nm}$ ) into the crystal at temperatures much greater than  $T_c$ . Thus, such *in situ* HRTEM analyses are capable of reveal-

ing the fundamental mechanisms governing the dynamic behavior of interphase boundaries in materials.

### Summary and Future Prospects

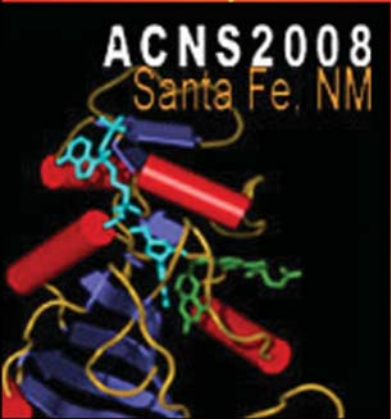
This article has demonstrated how *in situ* TEM and HRTEM can be used to understand the formation mechanisms of nanoscale materials, as well as many of their unique properties and dynamic behavior. It is extremely difficult, if not impossible, to obtain such information by any other technique. Having this information is essential to developing nanoscale materials and devices for various applications ranging from catalysts and field emitters to nanoelectronics and nanosensors. The time resolution of dynamic observations is currently limited by a combination of image signal and the image recording devices to about 0.03 s. Even with this limitation, *in situ* HRTEM is able to provide a wealth of information about detailed processes that occur at the nanoscale in materials. This situation will continue to improve as rapid progress is made in increasing the spatial, temporal, and chemical resolution of HRTEMs, in the capability of imaging devices, in storage and processing, and in precise computer control of the microscope. Other complementary spectroscopic techniques that were not mentioned in this article (e.g., electron energy-loss spectroscopy—see article by Saka et al. in this issue) can also be incorporated to follow chemical and/or bonding changes in materials *in situ*, offering many additional insights into nanomaterial phenomena. It is conceivable that it will be possible to image the three-dimensional structures of materials at or near the atomic level using energy-filtering TEM and/or high-angle annular dark-field scanning TEM and image reconstruction methods in the near future. Thus, it is anticipated that the role and capability of *in situ* HRTEM in nanoscience and nanotechnology will only continue to increase in the future.

### Acknowledgments

J.M.H. gratefully acknowledges Mr. Abhay Gautam, Dr. Kaushik Chatterjee, and Dr. Fritz Phillipp (MPI) for their collaboration on the Au-Cu work and support by the National Science Foundation under grants DMR-9908855 and DMR-0554792. Z.L.W. thanks the support from the National Science Foundation, Defense Advanced Research Projects Agency, and NASA. H.M. acknowledges Dr. Jung-Goo Lee (now at KIMS) for taking the images in Figures 1 and 2.

## References

1. J.-G. Lee, H. Mori, H. Yasuda, *J. Mater. Res.* **20**, 1708 (2005).
2. J.-G. Lee, H. Mori, H. Yasuda, *Phys. Rev. B* **65**, 132106 (2002).
3. T.B. Massalski, *Binary Alloy Phase Diagrams* (ASM, Ohio, 1986).
4. J.-G. Lee, H. Mori, *Philos. Mag.* **84**, 2675 (2004).
5. J.-G. Lee, H. Mori, *Proc. Materials Processing and Manufacturing Division Fifth Global Symposium*, S.M. Mukhopadhyay et al., Eds., 3 (TMS, Warrendale, 2004).
6. J.-G. Lee, H. Mori, *Phys. Rev. Lett.* **93**, 235501 (2004).
7. H.P. Poncharal, Z.L. Wang, D. Ugarte, W.A. de Heer, *Science* **283**, 1513 (1999).
8. H.Z.L. Wang, P. Poncharal, W.A. De Heer, *Pure Appl. Chem.* **72**, 209 (2000).
9. H.C.Q. Chen, Y. Shi, Y.S. Zhang, J. Zhu, Y.J. Yan, *Phys. Rev. Lett.* **96**, 075505 (2006).
10. H.X.D. Han, Y.F. Zhang, K. Zheng, Z. Zhang, Z.L. Wang, *Nano Lett.* **7**, 452 (2007).
11. H.X.D. Han, K. Zheng, Y.F. Zhang, Z. Zhang, Z.L. Wang, *Adv. Mater.* **19**, 2112 (2007).
12. H.P. Poncharal, C. Berger, Y. Yi, Z.L. Wang, W.A. de Heer, *J. Phys. Chem.*, **106**, 12104 (2002).
13. H.D. Golberg, P.M.F.J. Costa, O. Lourie, M. Mitome, X.D. Bai, Y. Bando, et al., *Nano Lett.* **7**, 2146 (2007).
14. X.D. Bai, D. Golberg, Y. Bando, C.Y. Zhi, C.C. Tang, M. Mitome, K. Kurashima, *Nano Lett.* **7**, 632 (2007).
15. J.Y. Huang, S. Chen, S.H. Jo, Z. Wang, D.X. Han, G. Chen, M.S. Dresselhaus, Z.F. Ren, *Phys. Rev. Lett.* **94**, 236802 (2005).
16. J.Y. Huang, S. Chen, Z.Q. Wang, K. Kempa, Z.F. Ren, et al., *Nature* **439**, 281 (2006).
17. H.J. Cumming, A. Zettl, M.R. McCartney, J.C.H. Spence, *Phys. Rev. Lett.* **88**, 56804-1 (2002).
18. Z.L. Wang, R.P. Gao, W.A. de Heer, P. Poncharal, *Appl. Phys. Lett.* **80**, 856 (2002).
19. W. Wei, Y. Liu, Y. Wei, K.L. Jiang, L.M. Peng, S.S. Fan, *Nano Lett.* **7**, 64 (2007).
20. R.P. Gao, Z.W. Pan, Z.L. Wang, *Appl. Phys. Lett.* **78**, 1757 (2001).
21. Z. Xu, X.D. Bai, E.G. Wang, Z.L. Wang, *Appl. Phys. Lett.* **87**, 163106 (2005).
22. Z. Xu, X.D. Bai, E.G. Wang, Z.L. Wang, *J. Phys.: Condens. Matter* **17**, L507 (2005).
23. J.C.M. Wayman, H.I. Aaronson, J.P. Hirth, B.B. Rath, Eds., *Metall. Mater. Trans. A* **25A**, 1781 (1994).
24. H.I. Aaronson, *Metall. Mater. Trans. A* **48A**, 2285 (2002).
25. J.W. Martin, R.D. Doherty, B. Cantor, *Stability of Microstructure in Metallic Systems*, 2nd Ed. (Cambridge University Press, Cambridge, 1997).
26. J.M. Howe, A.R.S. Gautam, K. Chatterjee, F. Philipp, *Acta Mater.* **55**, 2159 (2007).
27. W. Schweika, H. Reichert, W. Babik, O. Klein, S. Engemann, *Phys. Rev. B* **70**, 041401R (2004).
28. D.B. Butrymowicz, J.R. Manning, M.E. Read, *J. Phys. Chem. Ref. Data* **3**, 527 (1974).
29. J.M. Howe, W.E. Benson, *Interface Sci.* **2**, 347 (1995).
30. R. Sinclair, J. Morgiel, A.S. Kirtikar, I.-W. Wu, A. Chiang, *Ultramicroscopy* **51**, 41 (1993).
31. R. Kikuchi, J.W. Cahn, *Acta Metall.* **27**, 1337 (1979).
32. M. Sluiter, Y. Kawazoe, *Phys. Rev. B* **54**, 10381 (1996).
33. M. Asta, J.J. Hoyt, *Acta Mater.* **48**, 1089 (2000). □



## AMERICAN CONFERENCE ON NEUTRON SCATTERING

May 11-15, 2008

A meeting of the Neutron Scattering Society of America  
Eldorado Hotel & Spa  
Santa Fe, New Mexico, USA

**REGISTER NOW** for the American Conference on Neutron Scattering (ACNS2008) and experience a premier program on the high quality and breadth of neutron-related research across North America.

From fresh insights on macromolecules in motion, through shear-induced phase transformations in soft condensed matter, to materials for hydrogen storage, multiferroics, nanomagnetism and fundamental neutron physics... hear the latest research results. There will also be opportunities to dream and speculate about what's next on the Q-E map—the great unanswered scientific questions and novel instrument concepts.

**Session Topics include:**

- instrumentation and software
- polymers
- complex fluids
- biology
- chemistry and materials
- condensed matter physics
- engineering applications
- neutron physics

Register at [www.mrs.org/acns08](http://www.mrs.org/acns08) by May 2 for discounted rates.

For the most up-to-date information on ACNS2008 visit [lansce.lanl.gov/ACNS200](http://lansce.lanl.gov/ACNS200)